# In vitro measurements of hemodynamic forces and their effects on endothelial cell mechanics at the sub-cellular level

L. M. Lambert, I. I. Pipinos, B. T. Baxter, Y. S. Chatzizisis, S. J. Ryu, R. I. Leighton, and T. Wei

Citation: Biomicrofluidics **12**, 064101 (2018); doi: 10.1063/1.5028122
View online: https://doi.org/10.1063/1.5028122
View Table of Contents: http://aip.scitation.org/toc/bmf/12/6
Published by the American Institute of Physics

**Articles you may be interested in**

Biophysical analysis of fluid shear stress induced cellular deformation in a microfluidic device
Biomicrofluidics **12**, 054109 (2018); 10.1063/1.5063824

Layered acoustofluidic resonators for the simultaneous optical and acoustic characterisation of cavitation dynamics, microstreaming, and biological effects
Biomicrofluidics **12**, 034109 (2018); 10.1063/1.5023729

An integrated microfluidic platform for size-selective single-cell trapping of monocytes from blood
Biomicrofluidics **12**, 054104 (2018); 10.1063/1.5049149

Microfluidic platforms for rapid screening of cancer affinity reagents by using tissue samples
Biomicrofluidics **12**, 054108 (2018); 10.1063/1.5050451

# *In vitro* measurements of hemodynamic forces and their effects on endothelial cell mechanics at the sub-cellular level

L. M. Lambert,[1] I. I. Pipinos,[2] B. T. Baxter,[2] Y. S. Chatzizisis,[3] S. J. Ryu,[1] R. I. Leighton,[4] and T. Wei[1,a)]

[1]*Department of Mechanical & Materials Engineering, University of Nebraska–Lincoln, Lincoln, Nebraska 68588, USA*
[2]*Department of Surgery, University of Nebraska Medical Center, Omaha, Nebraska 68198, USA*
[3]*Cardiovascular Biology and Biomechanics Laboratory, Cardiovascular Division, University of Nebraska Medical Center, Omaha, Nebraska 68198, USA*
[4]*SRI International, Ann Arbor, Michigan 48105, USA*

(Received 7 March 2018; accepted 29 October 2018; published online 9 November 2018)

This paper presents micro-particle tracking velocimetry measurements over cultured bovine aortic endothelial cell monolayers in microchannels. The objective was to quantify fluid forces and cell morphology at the sub-cellular scale for monolayers subjected to steady shear rates of 5, 10, and 20 dyn/cm$^2$. The ultimate goal of this study was to develop an experimental methodology for *in vitro* detailed study of physiologically realistic healthy and diseased conditions. Cell topography, shear stress, and pressure distributions were calculated from sets of velocity fields made in planes parallel to the microchannel wall. For each experiment, measurements were made in 3 h intervals for 18 h. It was found that there is a three-dimensional change in cell morphology as a result of applied shear stress. That is, cells flatten and become more wedge shaped in the stream direction while conserving volume by spreading laterally, i.e., in the cross-stream direction. These changes in cell morphology are directly related to local variations in fluid loading, i.e., shear stress and pressure. This paper describes the first flow measurements over a confluent layer of endothelial cells that are spatially resolved at the sub-cellular scale with a simultaneous temporal resolution to quantify the response of cells to fluid loading. *Published by AIP Publishing.* https://doi.org/10.1063/1.5028122

## I. INTRODUCTION

Atherosclerosis is a cardiovascular disease responsible for over 26 000 deaths in the United States each year (https://www.nhlbi.nih.gov/files/docs/factbook/FactBook2012.pdf). It is a progressive disease in which cholesterol, fat, and other substances accumulate in the walls of arteries. This accumulation results in hardening of the arterial wall and constriction of the lumen, significantly reducing blood flow. In later stages, rupture or endothelial erosion of the plaques can lead to clot formation and subsequent stroke or myocardial infarction.

The fact that atherosclerosis typically occurs in the carotid, femoral, and coronary arteries, along with the abdominal aorta, is attributable to the complex vessel geometries that include bends and bifurcations, i.e., areas that have been associated with low mean wall shear stress. This is consistent with the findings of several studies[1–3] demonstrating that atherosclerosis has a strong preference to arterial regions experiencing low shear stress. It has further been shown[1,4–8] that areas of low shear stress also coincide with areas of high low-density lipoprotein (LDL) concentrations. LDL is a glycoprotein that transports lipids (i.e., cholesterol) within blood vessels. Specifically, cholesterol-carrying LDL can transmigrate the endothelial layer as a result of

a)Author to whom correspondence should be addressed: twei3@unl.edu

endothelial layer disruption, and the content within LDL can become oxidized leading to plaque growth in the arterial wall.[2,9,10] It is hypothesized that endothelium disruption is caused by a change in an endothelial cell's shape as it is subjected to different shear stresses, and the relationship between cell shape and shear stress can affect the localization of LDL transmigration and, therefore, atherosclerosis.

There have been significant advances in understanding the chemistry and biology of atherosclerosis at the cellular scale. It is, however, highly complex, and the ability to use this knowledge to treat the disease is still limited as discussed in recent overviews of the pathophysiology.[11–13] Effects of such factors as the recovery of the glycocalyx[14] and endothelial cell membrane fluidity[15] have been identified as important. The disease entails transmigration of LDL across the endothelium,[2] oxidation of LDL,[9,10] and transport and transformation of monocytes into macrophages which, after engulfing LDL, become foam cells.[16] There is also proliferation and migration of smooth muscle cells (SMCs), expression and breakdown of collagen, apoptosis of SMCs, endothelial cells (ECs), foam cells, etc., all of which aggregate to form plaques. There is also, in turn, micro-vascularization of the plaques, thrombosis, and formation of SMC caps over the plaque. Depending on a host of parameters, there can be plaque rupture leading to myocardial infarction, stroke, or simply formation of a new plaque at the same site.

That hemodynamics plays a significant role in the pathology of atherosclerosis is well known. It is known that plaques are most likely to form on the medial side of the daughter branch(es) of arterial bifurcations including the carotid artery, femoral artery, coronary arteries, and the abdominal aorta[17] leading to the femoral arteries. These regions are characterized by three-dimensional flow, low shear stress, and even flow reversals. Several studies have correlated atherosclerosis with regions of low shear stress.[1–3] Furthermore, high LDL concentrations have been found in areas of low shear stress.[3–8]

The first *in vivo* canine study of morphological responses associated with blood flow[18] found that endothelial cells (ECs) were elongated and parallel to blood flow in straight sections of a vessel and more randomly oriented and less elongated in the entrance regions of vessels. Furthermore, a slice of the canine thoracic aorta was rotated 90° to its original direction and then implanted in the aorta. After surgery, ECs of the implanted slice realigned in the flow direction. In another experiment,[19] the EC morphology and orientation in a rabbit aorta were found to be a likely indicator of the direction and speed of blood flow. These studies indicated a strong relationship between blood flow characteristics, EC morphology, and the genesis of cardiovascular disease.

Several subsequent *in vitro* experiments have been carried out to investigate the relationship between blood flow and cell morphology. Preliminary experiments showed that ECs in quiescent flow are polygonal in shape and exhibit "cobblestone-like" growth patterns.[20] *In vitro* experiments of steady, uni-directional flow over bovine aortic ECs[18] showed that cells aligned with the flow as well as elongated into ellipsoidal shapes. Additional studies[21–23] indicated that the morphological response to shear flow depended both on the magnitude of the applied shear stress as well as the duration of exposure to shear.

A later study[24] showed that the turbulent shear flow over ECs did not cause cell realignment or elongation. In yet another study,[25] including both laminar pulsatile and oscillatory flow, it was found that cells do align in pulsatile flow but not in the oscillatory case where there is no net bulk flow. *In toto*, the aggregate of these experiments indicated that ECs differentiate between different flow environments.

Although shear stress is often considered as the main hemodynamic force responsible for morphological and biological responses,[26–31] the forces perpendicular to the endothelial layer due to pressure can also be important.[26–29] *In vivo* variations in local blood pressure have shown to cause remodeling in vessels where the change in pressure was proportional to the rate of the vessel remodeling.[27] In addition, ECs that experienced increased normal forces acting on them due to osmotic pressure showed an increase in cell height with a reduction in external osmolarity.[26] Like studies mentioned previously, these experiments reiterate the need to investigate pressure and, moreover, perform investigations on the sub-cellular level in order to understand the complex relationship between cell remodeling and pressure.

What is not well understood is the integral coupling between vascular hemodynamics to cell biology, i.e., the mechanotransduction. This is, in large part, due to the mismatch in scales and the challenges of measuring flow parameters at the smallest, but biologically relevant, scales. The cell dynamics and biochemical reactions occur at scales of 1-10 $\mu$m, whereas the dimensions of plaques and arteries are on the order of $10^3$-$10^4$ $\mu$m, i.e., 0.1-1 cm. In order to know then, for instance, why or how an LDL molecule or a monocyte transmigrates the endothelium at a particular location, it is essential to know hemodynamic stress state precisely at the same resolution as the biology.

This shortcoming is widely recognized; a number of researchers have quantified cell morphology as a function of applied shear in *in vitro* experiments[32,33] and using computational fluid dynamics (CFD).[34] More recently, atomic force microscopy (AFM) was used to measure surface topography of ECs subjected to shear, and shear at the sub-cellular scale was then back calculated using CFD.[31,35,36] While this was a very important contribution, the coupling between mechanics and biochemistry remained elusive. Indeed, the vast majority of research involving shear stress effects on atherosclerosis has used the bulk shear in the vessel or, at best, the shear stress as a function of position on a plaque. Alternatively, computational shear stress data with sub-cellular resolution cannot be directly coupled with the cell biology.

To date, a comprehensive, fully integrated study specifically focused on simultaneous examination of cell biology and biomechanics of atherosclerosis at the sub-cellular scale has not been done. This is important obviously from gaining a complete understanding of the pathology of a disease with the highest mortality rates in the western world. However, with advances in drug treatments and therapies that can be precisely targeted into very specific locations, understanding precisely how to develop and where to deliver next generation therapies will be essential to successful control of this debilitating and deadly disease.

### A. Objectives

As noted previously, the ability to fully understand the mechanotransduction of atherosclerosis requires the detailed measurement of the hemodynamic stress distributions over endothelial cells on the same scale at which the biochemistry occurs; i.e., at the sub-cellular scale. The working hypothesis is that variations in both wall shear stress and pressure over individual cells play a critical role in both the mechanical as well as biological response of the endothelial layer to flow. The specific objectives of this investigation were

(i) to advance microfluidic measurements and processing methodologies to study mechanotransduction at the sub-cellular scale and
(ii) to quantify how stresses (wall shear and pressure) and topography evolve in response to applied flow.

## II. APPARATUS AND METHODS

This investigation entailed culturing a confluent layer of endothelial cells on the bottom wall of a micro-channel in quiescent media and subsequently applying a laminar steady flow. Mapping the velocity field at 3-h intervals from the onset of flow provided information about the temporal evolution of stress and topography for different applied flows. This section contains descriptions of the apparatus and methods used in this study.

### A. Micro-flow control system

The BioFlux™ 1000z (Fluxion Biosciences Inc.) is an integrated microscope/flow system suitable for measurements of this type. The flow control system utilized either BioFlux™ 24 or 48-well plates with embedded microchannels for *in vitro* flow assays, a pressure pump to drive the flow, an automated microscope stage to control three-dimensional acquisition location, and control software. The microscope stage could be positioned to an accuracy of 0.1 $\mu$m in each of the three coordinate directions. The system was calibrated for the microscope objectives so that

a 0.1 $\mu$m translation readout in the vertical direction corresponded to a true 0.1 $\mu$m distance in the microchannel. The stage also had a heating element that was used to keep microchannels and media at 37 °C.

As noted, the microchannels were manufactured by BioFlux™. In this study, 24-well plates were used to allow up to twelve simultaneous steady flow assays at applied shear stresses ranging from 0 to 20 dyn/cm$^2$. Flow was driven at a prescribed rate (i.e., shear) through a pneumatic pump that created a pressure difference across the upstream and downstream well of each microchannel. Note that the exit wells of the microchannels were at atmospheric pressure, and the upstream wells were held at whatever pressure was necessary to produce the desired flow rate (i.e., applied shear). For a flow with an applied shear of 20 dyn/cm$^2$, the pressure at the mid-length to the microchannel was ~0.1% higher than the pressure at the exit. For the range of flows studied in this investigation, the mean pressure at the mid-length of the microchannels were constant to better than 0.085%.

The microchannels had a rectangular cross section that was ~4000 $\mu$m long, 350 $\mu$m wide, and 70 $\mu$m high; these correspond to the $x$, $y$, and $z$-directions, respectively. The side and top walls of the microchannels were polydimethylsiloxane (PDMS). The bottom wall was glass and permanently fixed to the main PDMS plate.

### B. Micro-particle tracking velocimetry ($\mu$PTV)

Particle tracking velocimetry (PTV) is a standard flow measurement technique in fluid dynamics. It entails using a video camera to record sequences of flow seeded with small neutrally buoyant particles. For large-scale (e.g., aerodynamics) experiments, a sheet of laser light is typically used to illuminate the particles in a two-dimensional plane. Flow measurements with micrometer resolution (i.e., $\mu$PTV) are made using a camera mounted to a microscope; the microscope objective's focal plane defines the measurement plane. Video images are digitized and a computer algorithm computes displacements of every particle in the field of view from one frame to the next. By noting the location of each particle, this process yields a two-dimensional vector field, in which the flow velocity is measured at each particle location. Sub-pixel particle displacement resolution is achieved by finding the centroid of each particle image. Creating an ensemble of vector fields increases spatial resolution. Once the resolution is sufficiently high, a uniformly-spaced vector field can be created by interpolating the ensembled field.

Commercially available scientific cameras allow the user to specify the time between two successive video images (i.e., an "image pair"). This interval must be chosen to ensure that particle displacements between two consecutive video frames are small enough that individual particles can be unambiguously tracked, but large enough to minimize measurement uncertainty. For this study, a 12-bit, 1280 × 800 pixel resolution Phantom Miro M310 camera (Vision Research) was used. Flow was seeded with 1 $\mu$m diameter red Fluoro-Max fluorescent particles (Thermo Scientific); the specific gravity of these particles was 1.05. The time between images comprising each image pair was 1-3 ms; this corresponded to particle displacements of <10 pixels (~5 $\mu$m) from one frame to the next. High-resolution two-dimensional planar vector fields were then generated using ensembles of 3000 image pairs for every measurement plane.

The Bioflux system microscope, Nikon Eclipse Ti-S, was fitted with a CFI Super Plan Fluor ELWD 40× objective (Nikon Instruments Inc.) with a numerical aperture of 0.6 and a working distance of 2.8–3.6 mm. At this magnification, the spatial resolution in the $x$ and $y$-directions was 0.485 $\mu$m/pixel, and the nominal depth of focus, i.e., in the $z$-direction, was 1.5 $\mu$m.

The ability to accurately resolve topography, shear stress, and pressure at the cell surface, however, required much higher spatial resolution, particularly in the $z$-direction. Using an optical property of the seeding particles, the spatial resolution in the wall normal direction could be reduced down to ±0.15 $\mu$m. Specifically, because the particles were spherical and translucent, they would focus light like a lens. Consequently, in a thinner layer within the 1.5 $\mu$m depth of focus, the seeding particle images would appear as a dark ring with a bright center. Using image-processing techniques, only particles with a center that was brighter than a defined threshold would be used for $\mu$PTV measurements. The threshold for each set of measurements was selected to provide ±0.15 $\mu$m resolution in the $z$-direction. An example of this thresholding technique is shown in

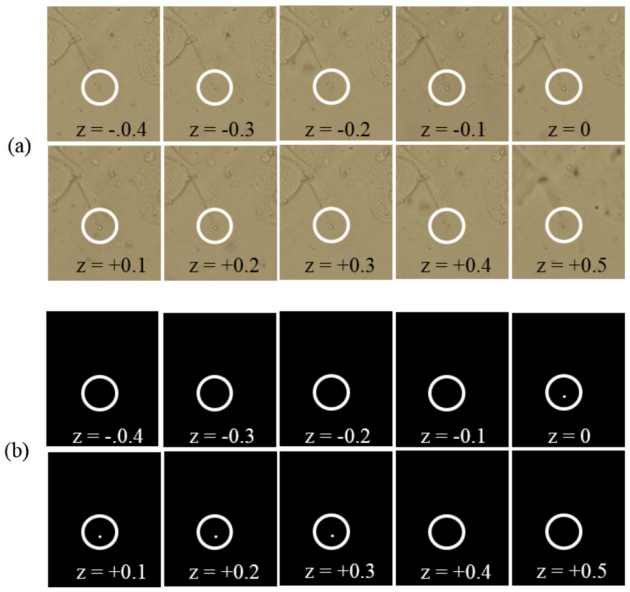


FIG. 1. A set of bright-field images showing a single stationary seeding particle resting on the channel flow imaged at $0.1\,\mu$m increments between $z=-0.4\,\mu$m and $z=+0.5\,\mu$m. (a) Raw images and (b) the corresponding processed image after applying an intensity threshold. The particle of interest has been circled in white. Observe that thresholding can reduce the thickness of the effective measurement plane to $0.3\,\mu$m.

Fig. 2. Figure 2(a) is a sequence of video images taken at $0.1\,\mu$m increments from $0.4\,\mu$m *below* the microchannel floor to $0.5\,\mu$m above, i.e., from being focused inside the glass to focusing in the microchannel. A seeding particle that had settled on the channel floor has been circled in white. Observe that at $z=-0.4$, $-0.3$, and $+0.5\,\mu$m, the particle image is a dark spot. In the range, $-0.2\,\mu\text{m}\le z\le+0.4\,\mu$m, the particle image is a dark ring with a bright center. By choosing an appropriate threshold, only the bright center of the particle image in the range, $0\,\mu\text{m}\le z\le+0.3\,\mu$m, remains. The bright spot is roughly circular with a diameter of 2-3 pixels. These are shown in Fig. 2(b). By computing the location of the centroid of that image, the center of the particle can be determined to better than 0.1 pixel accuracy.

For every profile measured in this investigation, the channel floor was found using the technique illustrated in Fig. 1. That is, the microchannels were first positioned so that the focal plane would still be inside the glass wall. The microscope stage would be moved in $0.1\,\mu$m increments until particles that had settled on the microchannel floor came into focus. By setting the appropriate threshold, a nominal $z=0$ wall location could be established. Note that this initial estimate would be to within $\pm0.15\,\mu$m of the wall where that particle was located; however, the actual cell surface location was computed from the $\mu$PTV velocity field measurements as described above.

Finally, a distinction should be drawn between accuracy of the microscope stage positioning system and uncertainty of the $z$-location of a seeding particle image. The former is assumed to be

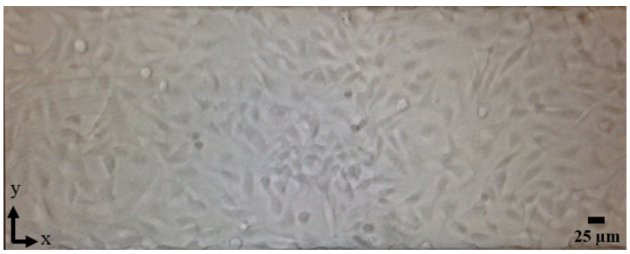


FIG. 2. Confluent layer of endothelial cells cultured in a microchannel immediately prior to initiating flow. The flow direction ($x$) is from left-to-right.

very accurate, such that a traverse of "n" steps of the positioning system in the $z$-direction would correspond to n/10 $\mu$m. Thus, in calculating derivatives in the vertical direction, the uncertainty in $dz$ due to the microscope stage is assumed to be zero. Given that particles carried by the flow could be anywhere within the 0.3 $\mu$m layer in which they would not be eliminated by thresholding, however, that uncertainty needed to be included in the derivative calculations.

### C. Endothelial cell culturing

Bovine Aortic Endothelial Cells (BAOECs) (Lonza Walkersville Inc.) were thawed and divided equally into eight 2 ml cryovials upon arrival and then stored at −70 °C for future use. One 2 ml cryovial of endothelial cells was needed for each flow experiment. The cells from the cryovial were subcultured onto three 100 mm tissue culture dishes (CytoOne) using Endothelial Cell Basal Media (EBM) including growth factors, cytokines, and supplements from the SingleQuots™ Kit. The cells in the tissue culture dishes were grown in an incubator at 37 °C supplemented with 5% $CO_2$. Cells were passaged three times, and each passage was subcultured onto three 100 mm tissue culture dishes. The third passage of cells was grown to 100% confluency before inserting the cells into the Fluxion BioFlux™ microchannels; the cells used in the study were the fourth passage.

Two different sets of experiments were conducted, one in which the cells were inserted into the microchannels and grown to confluency directly onto the glass floor, and the other where the microchannel floor was first coated with fibronectin. As will be discussed in Sec. III, there was virtually no difference between the two measurement sets.

For the experiments with the fibronectin coating, microchannels were first primed with Dulbecco's Phosphate-Buffered Saline (D-PBS) and then coated with fibronectin from bovine plasma (Sigma-Aldrich, St. Louis, MO) diluted in a D-PBS to a concentration of 100 $\mu$g/ml. (Fibronectin from bovine plasma is a multifunctional glycoprotein that has been shown to promote cell attachment in endothelial cells.[37]) The BioFlux™ plate was placed in the incubator (37 °C supplemented with 5% $CO_2$) for 1 h while the coating adhered to the channel. After 1 h, the microchannel was washed with D-PBS and then cells were inserted as described below. Since the fibronectin-coated channels used a very low concentration of fibronectin to coat the channels, the optical clarity was not affected.

For cell insertion, regardless of whether or not fibronectin was used, the solution of cells was divided evenly amongst the inlet wells of a 24-well BioFlux plate. The BioFlux 1000z pump was triggered for 2–3 s to pump the cell solution from the inlet wells to the outlet wells of the plate. After the pump was shut off, the suspended cell solution could be seen in the microchannels using the Nikon Eclipse Ti-S microscope. After cell insertion, the BioFlux plate was placed in the incubator (37 °C supplemented with 5% $CO_2$) for 2 h allowing the cells to adhere to the bottom surface of the microchannels. Once inserted, the cells were again grown to confluency. The entire culturing process typically took 6-10 days. Figure 2 is a photograph showing a confluent layer of ECs immediately prior to starting the flow.

### D. Flow conditions

Experiments were conducted at wall shear stress levels of 5, 10, or 20 dyn/cm$^2$ with and without fibronectin coating on the microchannel floor. The corresponding flow rates were 0.0245 ml/s, 0.049 ml/s, and 0.098 ml/s, respectively, and the Reynolds numbers, based on channel height and bulk velocity, were 2.66, 5.32, and 10.64. The working fluid was $CO_2$-independent media supplemented with L-glutamine and fetal bovine serum (FBS). This media solution helped one to maintain a pH of 7.2-7.4, while the experiment was conducted outside of an incubator and in the absence of 5% $CO_2$ supplementation. The density of the fluid was 0.993 gm/cm$^3$ and its dynamic viscosity was 0.0072 gm/cm s.

### E. Data acquisition

As noted in Sec. II B, flow was viewed in $x$-$y$ planes through the channel bottom. Measurements were made at eight different planes starting at the channel wall, i.e., $z = 0\,\mu$m, and 1, 2, 3, 4, 6, 8, and

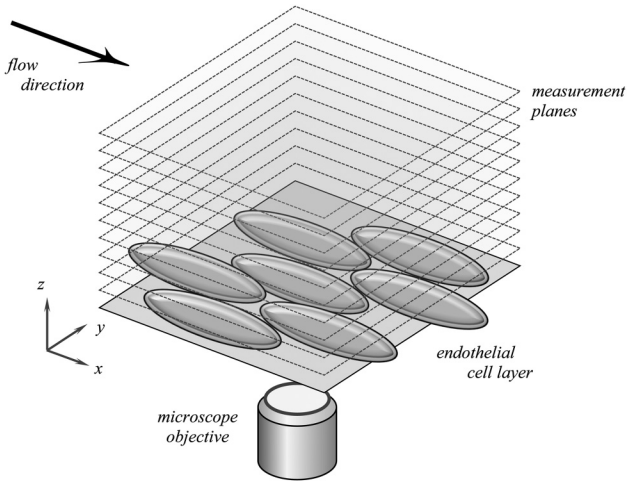


FIG. 3. Schematic depicting the measurement plane location with respect to the endothelial cells, imaging direction, and flow. Note that this schematic does not show the actual number of measurement planes and is not drawn to scale.

10 $\mu$m from the wall. This is schematically illustrated in Fig. 3. The bottom of the microchannel was found by positioning the focal plane, so the very few seeding particles resting on the bottom of the channel came into focus. Each measurement plane could be consistently and repeatedly located using the BioFlux™ software.

It is important to note that for all flow conditions, the flow speed was reduced to 0.0147 ml/s (3 dyn/cm$^2$) for $\mu$PTV video image capture. This was done to prevent phototoxic effects on the endothelial cells from high intensity light; it was found that measuring flow at speed required light intensities that caused vacuolization leading to necrosis. At a suitably low light setting, the camera exposure time needed to be longer to image the seeding particles, which, in turn, necessitated temporarily slowing the flow during image capture.

It is possible that lowering the speed may have had an effect on cell shape even if $\mu$PTV images were captured for only 7 min at a time every 3 h. It has been shown that there are biological responses to step changes in shear, including those involving the cytoskeleton, which occur on the time scale of minutes.[38–40] There are other changes, such as cell reorientation, which may take multiple hours to days to complete.[21–23] As such, slowing the flow for 7 min could be long enough for the fast responses to occur while being too fast for the slower responses to be significantly affected. As will be shown, there were clearing changes in cell morphology that could be resolved in these experiments. Further analysis to decouple the effects of "fast" and "slow" responses is a topic for subsequent study.

In addition, it is argued that the instantaneous flow field over the endothelial cells was set by the cell topography. Since the cell geometry did not change at this short time scale, the flow field along with the corresponding shear stress and pressure distributions over the endothelial cells was simply reduced by the appropriate ratio of either the flow rate or applied shear.

For all of the experiments, 3000 image pairs were recorded at each of the eight measurement planes on 3 h intervals beginning with the initiation of flow, $t = 0$, and continuing to the eighteenth hour. This allowed for the time resolved study of cell morphology and mechanical forces. Image pairs were captured at a rate of 80 Hz. One feature of the camera was that the time between images in an image pair, $\delta t$, could be set separately from the video-framing rate. This was varied as a function of how far the measurement plane was from the wall so that particle displacements between images in a pair were ~10 pixels. For the planes closest to the wall, a larger $\delta t$ was used; $\delta t$ was adjusted from 3125 $\mu$s closest to the wall to 1200 $\mu$s for the measurement planes 10 $\mu$m from the wall. The working field-of-view, i.e., the region of the microchannel in the camera field-of-view, was 466 $\mu$m × 349 $\mu$m. This corresponded to 960 × 720 pixel resolution in the $x$ and $y$ directions, respectively, or 2.06 pixels/$\mu$m in each direction.

### F. Image processing

Video images captured using the color Phantom Miro M310 camera during $\mu$PTV measurements were first converted to gray scale. As described in Sec. II B, a threshold was applied to the converted images to eliminate everything in each image except the seeding particles in a 0.15 $\mu$m thick plane. These were then converted to pure black and white.

An in-house $\mu$PTV program was then used to compute two-dimensional velocity fields for each set of 3000 video image pairs. Recall that there were 3000 image pairs acquired at each of eight measurement planes at 3 h intervals from $t = 0$–18 h. There are two major steps in the in-house $\mu$PTV program: (i) particle displacement analysis for each image pair and (ii) composite velocity averaging.

A brief overview of $\mu$PTV was provided in Sec. II B. The reader is referred to Lambert[41] for a detailed description of the specific algorithm developed for this study. For each $\mu$PTV image pair, the centroid of each seeding particle image was found, and the displacement between the particle centroid in the first frame and second frame was computed. To ensure that the particles were tracked unambiguously from one frame to the next, the user could specify a boundary within which the particle had to be found in the second frame relative to its location in the first frame. If the corresponding particle image was not found within that boundary in the second frame, no velocity for that particle was recorded. Similarly, if multiple particles were found within that boundary, velocity was also not measured. The computer was programed to search the entire $960 \times 720$ pixel field of view. Coordinates of each particle location and corresponding $x$ and $y$-velocity components were recorded.

Because of the low particle seeding density, each $\mu$PTV image pair produced a low spatial resolution two-dimensional velocity vector field at a specified distance from the microchannel wall. High spatial resolution was achieved by combining the 3000 vector fields obtained for each $z$-location and time. In this manner, roughly 85% of the $960 \times 720$ pixel locations had a unique instantaneous velocity measurement. A uniformly spaced vector field was then generated by averaging the velocity values inside $7 \times 7$ pixel windows so that there was an averaged velocity measurement every seven pixels in both the $x$ and $y$-directions. An estimate of velocity measurement uncertainty for this technique begins with the observation that seeding particle images were nominally circular bright spots with a diameter of 2-3 pixels. By computing the centroid of those images, the particle location could be determined to better than 0.1 pixel accuracy. With this resolution and the ~10 pixel displacement in a $\mu$PTV image pair, the measurement uncertainty of each individual velocity vector was at least 1%. As noted above, there were a minimum of 42 individual velocity vectors (i.e., 85%) in every $7 \times 7$ pixel window. Assuming the ergodic hypothesis, that the average will converge to the true value, the uncertainty for the ensemble averaged velocity in each window is then conservatively better than 0.005 pixels. Recalling that the time between images, $\delta t$, in a $\mu$PTV image pair was 3125 $\mu$s for measurement planes closest to the wall, and 1200 $\mu$s for measurements taken at $z = 10\,\mu$m, the uncertainty of the averaged velocities in each $7 \times 7$ pixel window was then <0.75 $\mu$m/s for measurements closest to the wall and <2 $\mu$m/s for measurements farthest from the wall. These uncertainties correspond to ~0.2% and 0.05% of the mean streamwise velocity at $z = 1\,\mu$m and 10 $\mu$m, respectively. This accuracy was essential for resolving surface topography and, more importantly, surface pressure.

A zoomed in region of a $\mu$PTV vector field is shown in Fig. 4. This figure is an overlay of the vector field over the top of the gray-scale cell images. This segment is ~98 $\mu$m in the streamwise direction and ~91 $\mu$m in the cross stream direction. Velocity magnitudes are indicated both by vector length and color; a color scale is included to the right. This particular vector field was taken 3 $\mu$m above the wall. Note that the r.m.s. cell heights are only ~1 $\mu$m. As such, the transverse velocities are very small and not visible in the figure.

Observe the dark region left of center in the image. This is an endothelial cell nucleus which extends farther out into the flow than the rest of the cell. For this reason, the velocity measurements over the nucleus are lower than the surrounding regions where the distance between the cells and the measurement plane is greater. This made it possible to accurately measure cell surface topography as will be described in Sec. II G.

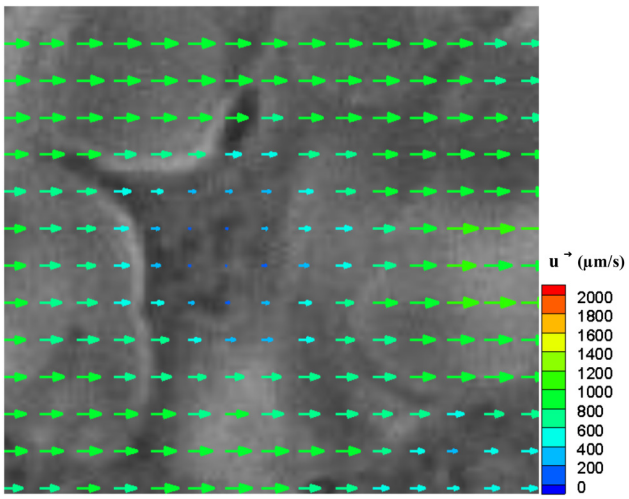


FIG. 4. A 98 $\mu$m × 91 $\mu$m segment of a $\mu$PTV velocity vector field overlaid on an image of endothelial cells. Flow is from left-to-right, and the measurement plane was located at $z = 3\,\mu$m above the wall.

### G. Shear stress and cell surface topography

The end result of computing all of the thousands of $\mu$PTV image pairs was a set of three-dimensional arrays with $138 \times 103 \times 8$ two-dimensional velocity vectors ($u$ and v) in the stream, transverse and wall normal directions, respectively. There was one such array for every 3 h interval for each of the three different flow conditions; see Fig. 3 for a schematic drawing illustrating the three dimensional array.

Note, then, that for every vector location, $(i, j)$, and time, $t = T$, there was a velocity profile, $u_{i,j}(z,T)$. By computing the zero intercept of that profile, i.e., the value of $z_o$ at which $u_{i,j}(z_o,T) = 0$, the endothelial cell height at that location was found; this is simply a mathematical statement of the standard "no-slip" condition at a solid boundary. Because there was a unique velocity profile at every vector location in the field-of-view at every 3-h time interval, it was possible to generate three-dimensional surface contours of the endothelial cell layer as a function of time.[28,42]

In addition, the local wall shear stress was computed simply from the definition

$$\tau_o = \mu\, \partial u/\partial z \tag{1}$$

evaluated at the now known wall location, $z_o$. In actuality, a first-order polynomial was fit through the velocity profile to obtain a more accurate value of the wall shear.[28,42] This was done because the velocity profile within 10 $\mu$m of the wall is essentially linear. Using a higher order polynomial fit creates the possibility of non-physical higher order harmonics which would introduce numerical error in both the cell surface and wall shear stress calculations.

It should be pointed out that there were two velocity gradient calculations used in this study. The first was calculating the mean gradient for the purpose of determining the wall shear stress as described in the preceding paragraph. The second was calculating the local gradients for use in the wall pressure calculations. Using the ensemble averaged velocity uncertainty of ~2 $\mu$m/sec at $z = 10\,\mu$m, the uncertainty of the mean velocity gradient was 0.2 $s^{-1}$ which corresponds to a wall shear stress uncertainty of ~0.0014 dyn/$cm^2$. This is 0.05% of the 3 dyn/$cm^2$ at which the flow measurements were made.

The uncertainty of the local velocity gradients was determined from the 0.75 $\mu$m/s near wall velocity uncertainty and, using central differencing, 2 $\mu$m between adjacent measurement planes. The propagation of uncertainty in the sum or difference of two numbers is the square root of the sum of the uncertainties squared. This results in a local gradient uncertainty of 0.53 $s^{-1}$ or a local shear uncertainty of ~0.0038 dyn/$cm^2$. This is 0.13% of the 3 dyn/$cm^2$ applied shear at which

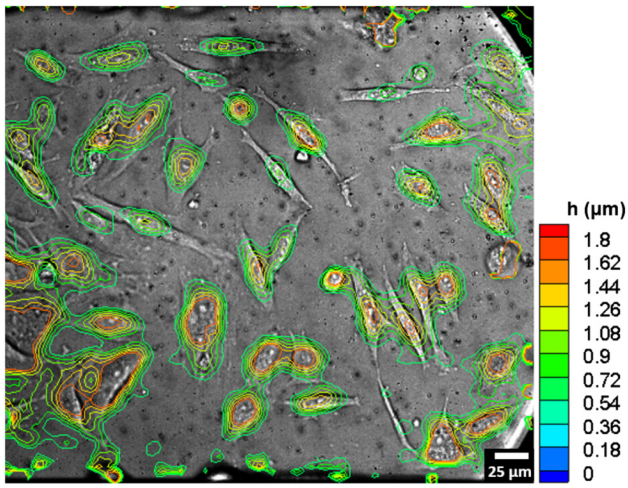


FIG. 5. Cell surface contours computed for a non-confluent layer of necrotic bovine aortic endothelial cells for the 18th hour while subjected to an applied shear stress of 20 dyn/cm$^2$. The measurements validate the cell surface height measurement methodology.

measurements were taken. To demonstrate the power and accuracy of these measurements, a sample surface contour plot overlaid on the corresponding cell image is shown in Fig. 5. It is important to recognize that this particular measurement turned out to have been taken for an endothelial cell culture that was not confluent and, in fact, was undergoing vacuolization as a result of phototoxicity. The key feature of this figure, however, is the exact matching of cell topography with the cell images. Observe also that the maximum height of the cells was <2 $\mu$m demonstrating the ability to resolve cell topography at the submicron level; the same ±0.15 $\mu$m uncertainty in the measurement plane location would carry over to the uncertainty for cell height calculations.

Before proceeding to the wall surface pressure calculations, it is worth noting additional features included in the post-processing routine. In particular, additional routines were developed for the $\mu$PTV velocity vector fields to improve measurement accuracy and to correct for microchannel tilt. Erroneous vectors were identified and removed using a local median test.[43] It should be pointed out that the routine was written such that great care was put into eliminating error sources in the processing algorithm. As such, there would be roughly only one vector out of ~200 vector *fields* identified by the error detection algorithm. With that low rate, the *entire* vector field would be discarded rather than develop an *ad hoc* correction algorithm. Details of the specific application to this $\mu$PTV algorithm are provided in Lambert.[41]

A more challenging problem was that the measurement system was capable of sensing even very small angles of tilt in the microchannel relative to the microscope viewing plane. That is, the Bioflux plate did not sit perfectly flat on the microscope stage to within less than a micrometer. This manifested itself as a linear velocity gradient across the camera field-of-view.

The positive aspect of this problem is that it validates the ability to use $\mu$PTV velocity measurements to accurately compute cell height variations on the order of fractions of a micrometer. The downside was that when the microchannel was tilted relative to the Bioflux microscope stage even by only 1-2 $\mu$m, the measured two-dimensional velocity field would appear to have a uniform gradient. For reference, the maximum observed tilt was ~5 $\mu$m across the ~900 $\mu$m field-of-view, i.e., <0.32°.

Given that the height of endothelial cells was <3 $\mu$m, a tilt correction algorithm was necessary.[41] In brief, the cell surface height algorithm, described previously in this section, was used to compute the uncorrected surface topography. From this calculation, a locus of local surface minima was found. These nominally correspond to locations in the field-of-view where the endothelial cells were very thin, or where there were small areas with no cell coverage on the microchannel floor. A planar surface was then fit to this locus of minima. This defined the position of the tilted channel floor relative to the microscope measurement plane. By subtracting this tilt plane from the uncorrected surface topography, a tilt-corrected topography was produced.

### H. Computing wall pressure from μPTV data

One of the great strengths of these μPTV measurements was the ability to compute surface pressure distributions from the velocity field data. While this is something that is routinely done in computational studies, this has never been done in actual measurements over live endothelial cells. In principle, if one has the fluid velocity field in a region, the Navier-Stokes equations can be integrated to extract the pressure field.

In practice, because the Navier-Stokes equations are non-linear second order differential equations, even the smallest amount of noise in the measured velocity field can cause large errors in the pressure calculation. Recently, there have been a number of investigators who have made significant strides in resolving this problem, most notably, Dabiri *et al.*[44] Solution approaches of these types are being developed center around the statistical randomness of the noise rather than trying to somehow remove it.

In this study, the *x*-component of the Navier-Stokes equations, written here with the pressure gradient term isolated on the left hand side,

$$\partial P/\partial x = -\rho(U\partial U/\partial x + V\partial U/\partial y + W\partial U/\partial z + \mu(\partial^2 U/\partial x^2 + \partial^2 U/\partial y^2 + \partial^2 U/\partial z^2), \quad (2)$$

was integrated in the *x*-direction across the field-of-view (from left-to-right) for every spanwise location, *y*.

Close to the wall, the uncertainty in velocity is 0.2% (0.75 μm/s) and the uncertainty of wall normal velocity gradients is 0.13% (0.53 $s^{-1}$). Uncertainties in velocity gradients computed in the *x* and *y*-directions are 3.4 times smaller than the wall normal gradients because the vector spacings in the horizontal directions are 3.4 μm compared to the 1 μm vertical spacing. The uncertainties of products sum and the uncertainties of sums and differences are equal to the square root of the sum of the squares of the component uncertainties. Finally, since the wall normal velocity, *W*, was not measured, the uncertainty of the pressure gradient was 0.39%.

Integration is a summing process. Therefore, the uncertainty in integrating pressure from one *x*-location to the next is $\sqrt{2}$ times the uncertainty of the pressure gradient (since integration is a summing process). This is 0.55%. The reference is the applied shear stress at which measurements were made, i.e., 3 dyn/$cm^2$, so the pressure uncertainty is 0.017 dyn/$cm^2$. Even with this level of uncertainty, it is important to keep in mind that the pressure variations over the cells due to viscous effects will also be very small. As such, particular attention must be paid to error propagation in these calculations.

There are, in general, two types of errors, random and systematic. By definition, random errors will statistically average out to zero. In the pressure field calculations, one would expect to see them, if they were significant, as comparatively large amplitude, high wave number fluctuations on top of the true pressure signal. Indeed, without a highly resolved velocity field, this random error would result in meaningless pressure calculations. Systematic errors, on the other hand, would propagate in the direction of integration and create potentially large-amplitude, low wave-number oscillations.[41] Depending on their orientation, cells in this study spanned roughly ten or more vector spacings in the *x*-direction. Thus, the wavelength of random errors would be much shorter than the typical cell dimension, and the extent of any systematic errors would be significantly longer. That is, it would be possible to recognize the presence of error in the calculated pressure fields.

Examination of the raw pressure calculations showed no significant random error. There was, however, a low wavelength variation in the pressure field characteristic of systematic error. The amplitude of these variations was less than 1 dyn/$cm^2$ with a wavelength that spanned the entire field of view. This systematic error was removed by fitting a low wave-number spline along lines of constant *y* and subtracting this spline from the corresponding calculated pressure. The difference, then, was the actual pressure variation in the *x*-direction for each *y*-location. Applying this method for every row ($y$ = constant) in the field-of-view resulted in the pressure field shown in Fig. 6. This is a set of four plan-view (i.e., *x*-*y* plane) images showing the endothelial cells, Fig. 6(a), along with overlaid contour plots of shear stress, topography, and wall pressure, Figs. 6(b)–6(d), respectively.

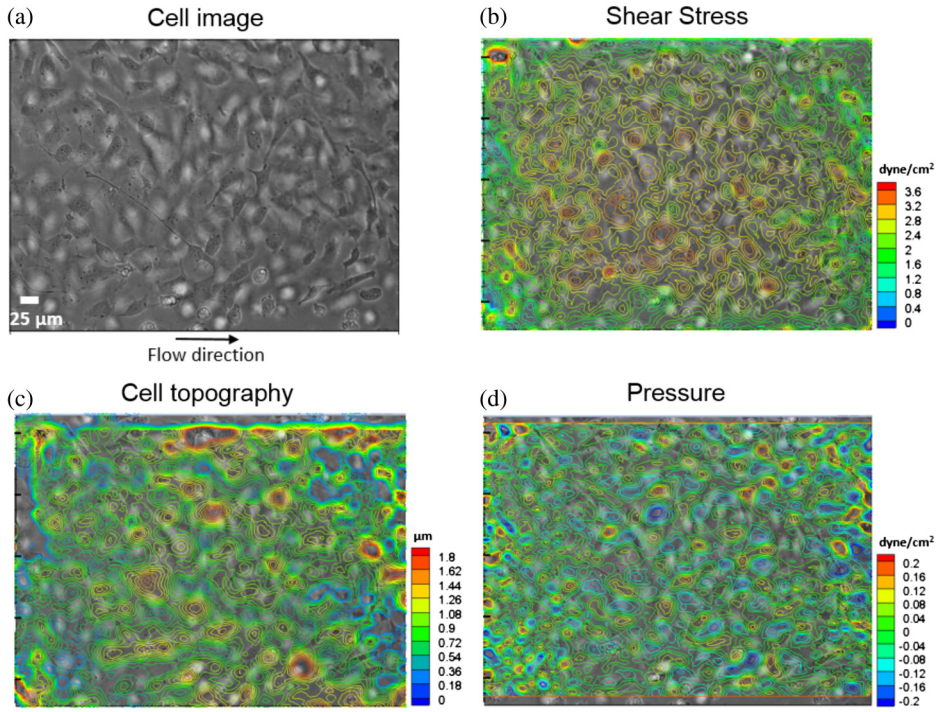


FIG. 6. Plan view image of confluent BAOECs (a), with the corresponding shear stress (b), cell topography (c), and pressure contour plots overlaid. Measurements were for confluent endothelial cells cultured on glass at the 0th hour time step with an applied shear stress of 10 dyn/cm$^2$. Flow is from left to right.

### I. Cell averaging

Another advantage of this experiment was the ability to simultaneously study a number of cells subject to the same environment. While the possibility existed, therefore, to examine the response of each cell individually, there was equal if not greater value in looking at an ensemble of cells to develop a statistical sense of the response of the cells to applied shear over time. The method for doing this is described in the following paragraphs.

As can be seen in Figs. 2 and 6, in each experimental run, there were multiple endothelial cells in the field-of-view of each microchannel. A MATLAB edge detection algorithm was developed to find the cell boundaries in each microchannel for the three different shear cases. The cell boundaries found using the edge detection algorithm were compared visually with the corresponding raw video microscope image. In addition, key features of the cell, e.g., cell boundary, nucleus, etc., had to be visually identifiable and whether the cell boundaries from edge detection algorithm and visual inspection coincided. For each of the three shear cases, there were at least fifteen cells which were unambiguously identified.

For each of the selected cells, then, the maximum streamwise length, $L$, and cross-stream width, $W$, were measured. Each cell had its unique values of $L$ and $W$ along what was then referred to as the cell's major and minor axes. Using dimensionless coordinates, $x/L$ and $y/W$, mean variations of biomechanical parameters, i.e., topography, shear stress, and wall pressure, over the sample of fifteen cells could be computed. The ensemble averages for shear stress and pressure were then normalized by the maximum shear stress at the 0th hour for each flow case so that shear stress and pressure variations could be compared. Data in Sec. III are ensemble-averaged results.

## III. RESULTS AND DISCUSSION

Measurements of flow over a confluent layer of live bovine endothelial cells were made at three different shear stresses, 5, 10, and 20 dyn/cm$^2$, with endothelial cells cultured directly on

the untreated glass microchannel floor. Experiments were also conducted at 5 and 20 dyn/cm$^2$ with the floor coated with fibronectin. For all cases, $\mu$PTV measurements were initiated at $t = 0$, when the flow was turned on, and continued at 3 h intervals for 18 h. As explained in Sec. II B, and discussed later, there were no significant differences between the data sets with and without fibronectin. As such, only the more complete data set from the untreated channel is presented here.

An argument has been made that endothelial cells change shape in response to increasing shear in a manner that reduces their overall drag.[28,45] This implies that cells reduce in height with increasing shear and take a more wedge-like shape with the highest part of the cell moving to the back half of the cell. At the same time, it would be expected that the maximum shear stress over the top of the cells would decrease and that there would be an overall reduction in total shear force acting on the cell. The other finding[28] was that the surface pressure variations over endothelial cells were of the same order of magnitude as the shear stress variations. In that study, measurements were made over fixed endothelial cells. The present study allows for direct examination of pressure for a confluent layer of live cells subject to a range of applied shear stresses. These results and discussions of biological implications are presented in Secs. III A and III B.

### A. Temporal evolution of endothelial cell shape

The first issue to be addressed was whether and how endothelial cells change shape in response to applied shear. Using the method described in Sec. II G, the mean or averaged cell height along the streamwise centerline passing through the maximum cell height was computed for each 3 h time interval over the 18 h experiment. This was done for all three applied shear cases.

Figure 7 shows the averaged cell height profile computed for each time step for a confluent layer of endothelial cells cultured on glass at an applied shear stress of 10 dyn/cm$^2$. Each curve is the average height of the fifteen selected cells at the non-dimensionalized streamwise locations, $x/L$. The leading edge of the cells was located at $x/L = 0$ and the trailing edge was at $x/L = 1$. Seven separate curves are shown, one for each time interval from $t = 0$ to $t = 18$ h. Each time interval is indicated in the plot legend.

The important features of the curves in Fig. 7 are that the maximum cell height decreases and the location of the maxima moves downstream with time. The solid line denoting averaged cell height at the onset of flow indicates that the cells have an average maximum height of 1.61 $\mu$m

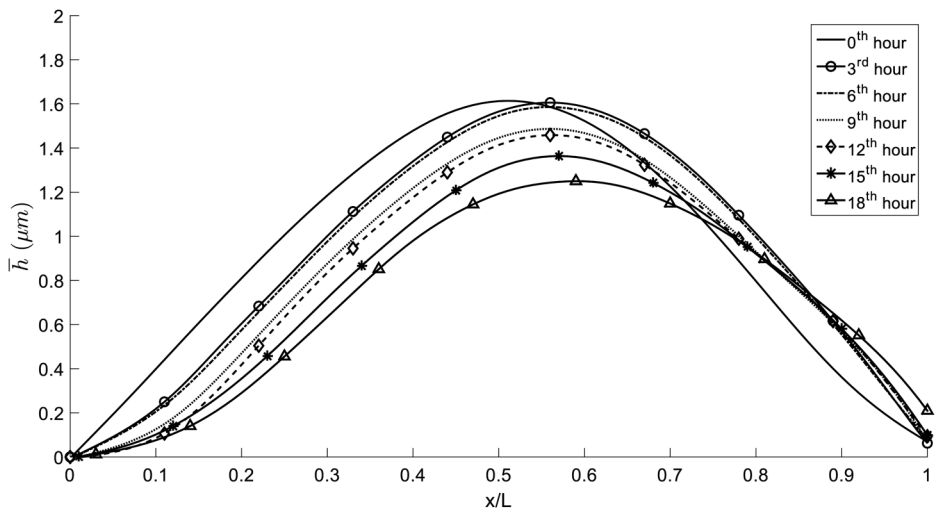


FIG. 7. Average cell surface height along the normalized streamwise cell position for the 3 h time intervals following initiation of flow. For these data, endothelial cells were cultured on glass and subjected to a shear stress of 10 dyn/cm$^2$.

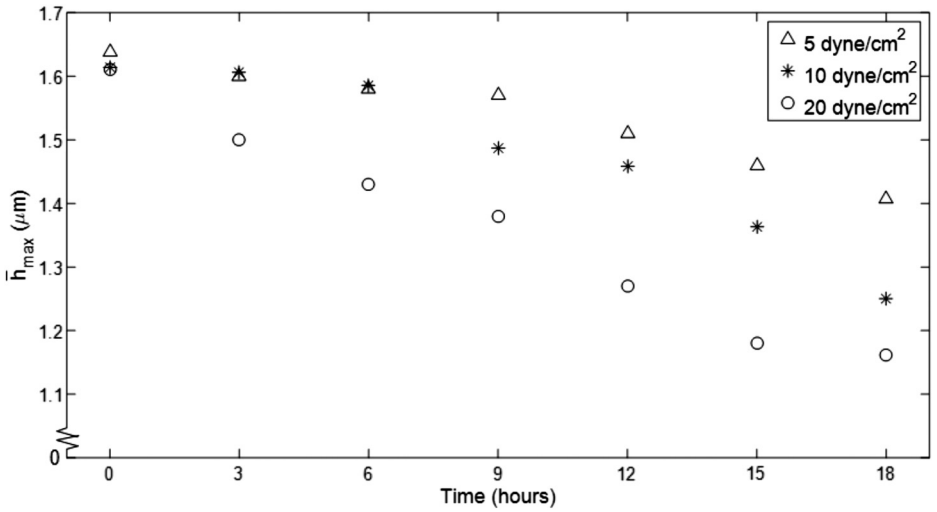


FIG. 8. Maximum cell surface height measured as a function of time for endothelial cells cultured on glass at applied shear stresses of 5, 10, and 20 dyn/cm$^2$.

located about the center of the cells, $x/L = 0.51$. There is a monotonic, albeit not linear, trend in which the maximum cell height decreases and moves downstream with time. After 18 h, denoted with triangles, the mean maximum cell height is 1.23 $\mu$m, ~23% lower than the initial maximum height. As seen in Fig. 7, the location of that maximum is at $x/L = 0.59$.

A summary of the main findings for all three applied shear stresses, 5, 10, and 20 dyn/cm$^2$, is shown in Figs. 8 and 9. Figure 8 shows the change in maximum average cell height, while Fig. 10 shows the location of maximum height. For both plots, then, the abscissa is time, $t$, relative to when flow (i.e., steady shear flow) was first initiated. Observe in Fig. 8 that the trend of decreased maximum cell height with time is visible for all three applied shear stresses. Similarly, in Fig. 9, the change in cell shape, with the point of maximum height moving downstream with time, also occurs in all three cases.

What is probably the most important point to remember about the cell height variations is encapsulated in Fig. 10, which shows the averaged cell height distributions for the three applied

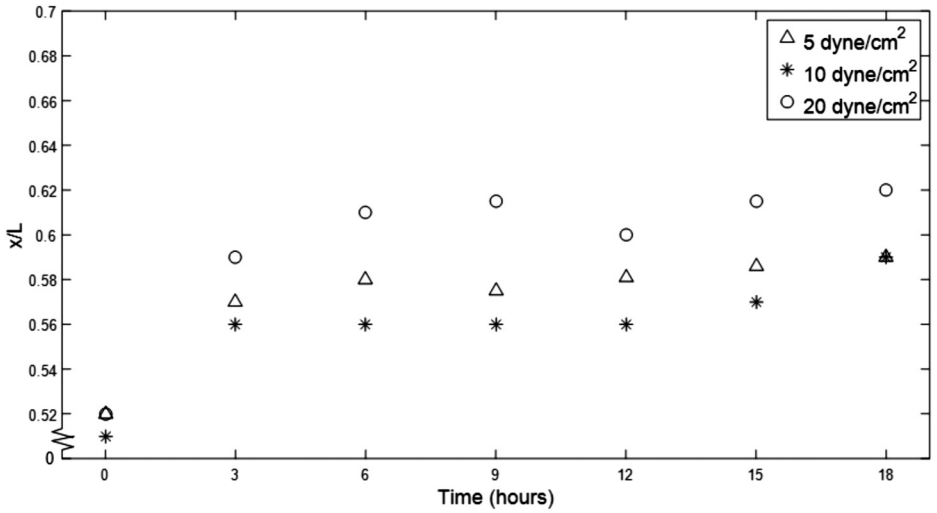


FIG. 9. The normalized streamwise location of maximum cell height measured at each 3 h time interval for endothelial cells cultured on glass at applied shear stresses of 5, 10, and 20 dyn/cm$^2$.

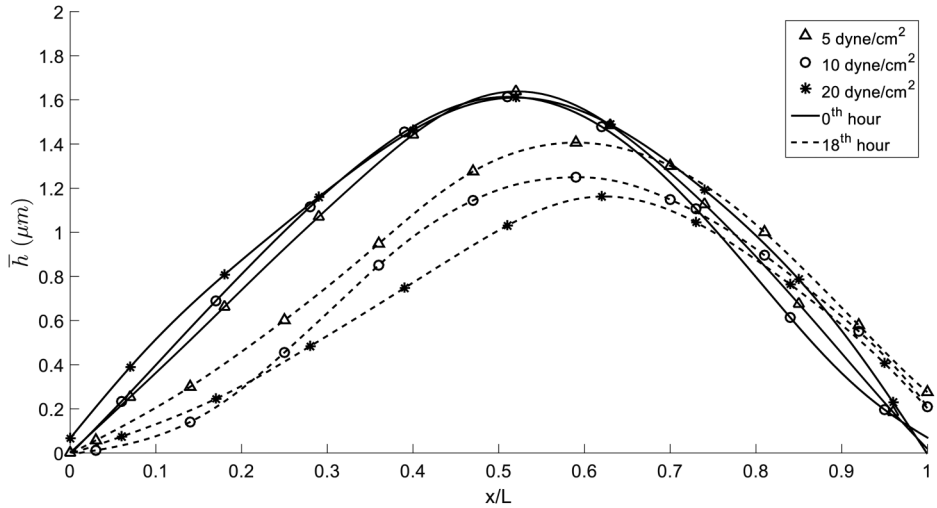


FIG. 10. Average cell surface height variations along the normalized streamwise cell length at the 0th and 18th hour time steps for endothelial cells cultured on glass.

shear cases at the 0th and 18th hours. The format of this figure is identical to that of Fig. 7. In Fig. 10, however, the three solid lines show the initial averaged cell height distribution along the cells at the initiation of flow, and the dashed lines indicate the cell heights after 18 h. The three plotter symbols, triangles, circles, and asterisks, correspond to the 5, 10, and 20 dyn/cm$^2$ cases, respectively. Observe first that at the onset of flow, the cell shapes for the three cases are not appreciably different, nor would one expect them to be. They all show a maximum height of $\sim$1.6 $\mu$m located at the mid-point along the cells.

What can also be seen in Fig. 8 is that the maximum cell height 18 h after flow was started is lower for higher shear levels. The maximum cell height values are 1.4 $\mu$m, 1.23 $\mu$m, and 1.18 $\mu$m for the lowest to highest applied shear stresses. The standard deviation of these measurements was $\pm$0.15 $\mu$m. Similarly, the degree to which the highest point of the cells is pushed downstream also increases with increasing applied shear as seen in Figs. 9 and 10.

These findings are consistent with the expectation that endothelial cells will change shape in such a way as to reduce the hemodynamic drag forces they experience from the flow. They are also consistent with AFM measurements[46,47] that observed this same morphological response when cells are subjected to shear. The maximum cell height at 20 dyn/cm$^2$ found in this study, $1.2 \pm 0.15$ $\mu$m, virtually matched the measurements of Ohashi *et al.*[46] who found a maximum cell height of $1.2 \pm 0.4$ $\mu$m. It was somewhat different from, but still consistent with measurements from Barbee *et al.*'s[47] measured value of $1.8 \pm 0.7$ $\mu$m. The significant new contribution here is the ability to track the morphology with time over a live endothelial cell layer.

It is expected that the net volume of each endothelial cell should remain constant, even though the cell changes shape in response to applied shear.[45,48] The only reason the volume would change would be if there was a change in the osmotic balance of the cell due to ion transport; this did not occur in these experiments. In order for volume to be conserved, the reduction in cell height in the streamwise direction must be accompanied by a concomitant spreading of the cell in the lateral direction. From the most simplistic of perspectives, if the cells cultured in a quiescent fluid can be thought of as semi-ellipsoidal in shape, then the end geometry after application of shear changes their shape into something more closely resembling a wedge. The point is that the reduction in height along the cell centerline must be accompanied by an increase in height along the sides of the cells.

This spanwise change in morphology in response to shear is shown in Fig. 11. In this figure, the variation in the average cell surface thickness, $h$, is shown with respect to normalized spanwise position, $y/W$, along the cell, where $W$ is the maximum cell width. As in Fig. 9, solid lines depict the mean cell height at the 0th hour and the dotted-lines are for the 18th hour.

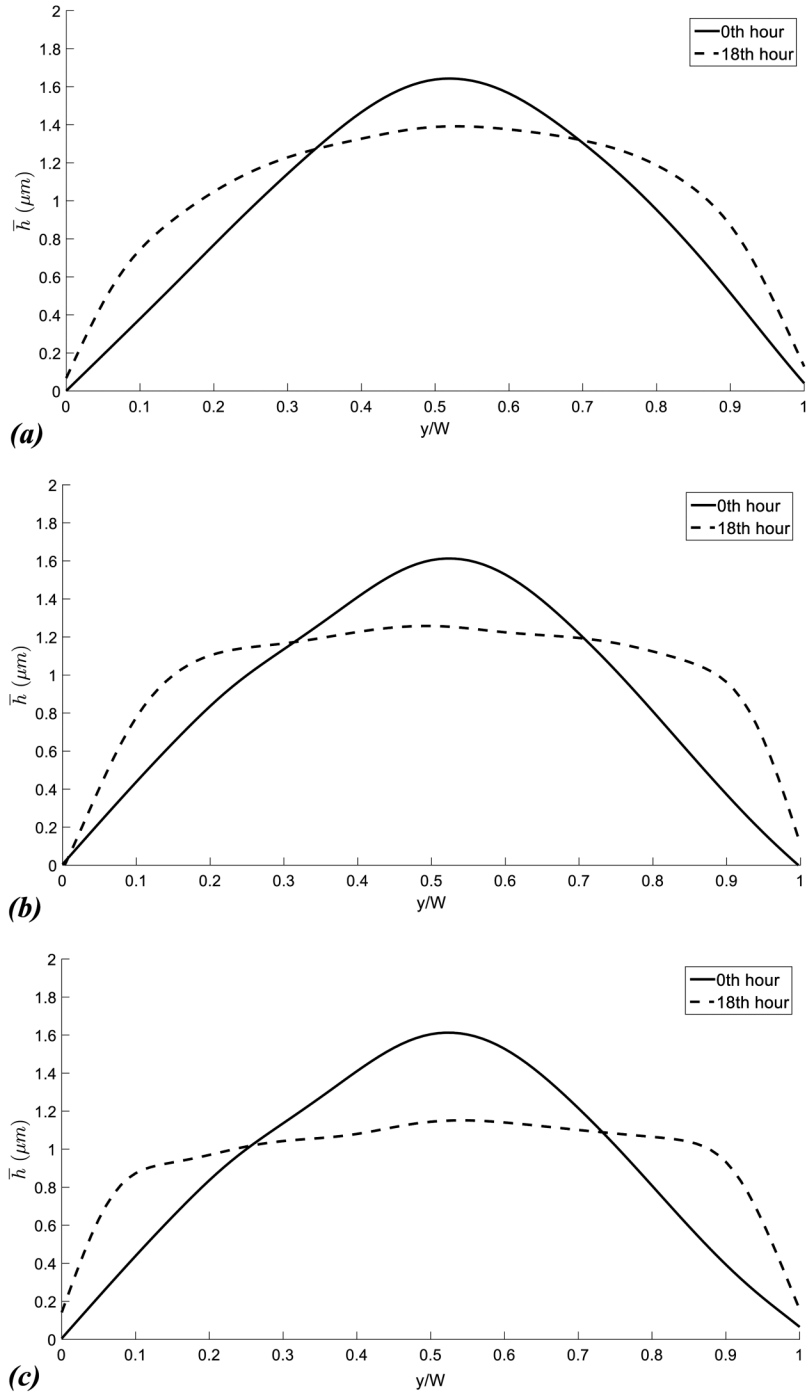


FIG. 11. Average cell surface height as a function of non-dimensional spanwise direction, *y/W*, at the 0th and 18th hour for (a) 5 dyn/cm$^2$, (b) 10 dyn/cm$^2$, and (c) 20 dyn/cm$^2$. Data are for cases where the endothelial cells were cultured on glass.

By way of reference, the maximum cell heights of the spanwise topography in Fig. 10 are the same as the maximum cell height of the streamwise topography values for each applied shear stress shown in Figs. 8 and 10. This was expected because both the streamwise and spanwise height profiles were taken with respect to the location of maximum cell height. The critical feature of Fig. 11 is that while the cell height decreased near the center of the cell, it increased laterally

over the 18 h of applied shear. This is consistent with the expectation that the cell volume for these experiments will remain constant.

### B. Shear stress and pressure variations

The key findings of the shear stress analysis for flow experiments at 5, 10, and 20 dyn/cm$^2$ are highlighted in Fig. 12. This figure shows streamwise variation in average shear stress for the three different applied shear levels at the 0th and 18th hours. The plotter symbols and line convention are the same as that used in Fig. 10. For ease of comparison, the averaged local shear stress values were normalized by the maximum local shear (i.e., where the cell height was a maximum cell) at the 0th hour. This was also done to account for the fact that the flow speed during $\mu$PTV measurements was reduced; this was discussed in Sec. II E.

As would be expected, the change in cell topography is accompanied by a change in shear stress magnitude and distribution over the 18 h span. As seen in Fig. 12, at the 0th hour, shear stress is symmetric about the half-length, $x/L = 0.5$, of the cells. Over a period of 18 h, the location of the maximum shear stress, like the location of maximum height, shifts downstream. Indeed, the location of maximum shear logically coincides with the location of maximum height. This is consistent with findings of a number of other studies.[35,46–48]

The largest applied shear causes the greatest change in both cell geometry as well as shear. For the three different applied shears, 5, 10, and 20 dyn/cm$^2$, the maximum normalized local shear stress values, $\tau_{max}/\tau_{0hr\text{-}max}$, were 0.70, 0.52, and 0.39, respectively. The corresponding reductions in maximum shear stress at the thickest part of the cell were then 30%, 48%, and 61%. The standard deviation of the measurements was ±0.21. These results are consistent with the finding[38] that shear stress decreases with a decrease in cell height for the same applied shear rate.[49–52]

The maximum shear stress values are, however, lower than those obtained in computational studies.[36,52] In those studies, atomic force microscopy (AFM) or fluorescence imaging was used to measure cell topography and, in turn, generate computational grids for the endothelial cells. The computational results showed maximum shear stress values as high as three times that of the average applied shear of 10 dyn/cm$^2$. At the same time, the measured cell heights also appeared to be approximately three times greater than the current measurements. It may be that the sub-cellular resolution in the current study is lower than that of the computational studies. At the same time, the computational studies, though starting with live cells, immediately lose the dynamic response when the investigation transitions to the computational domain.

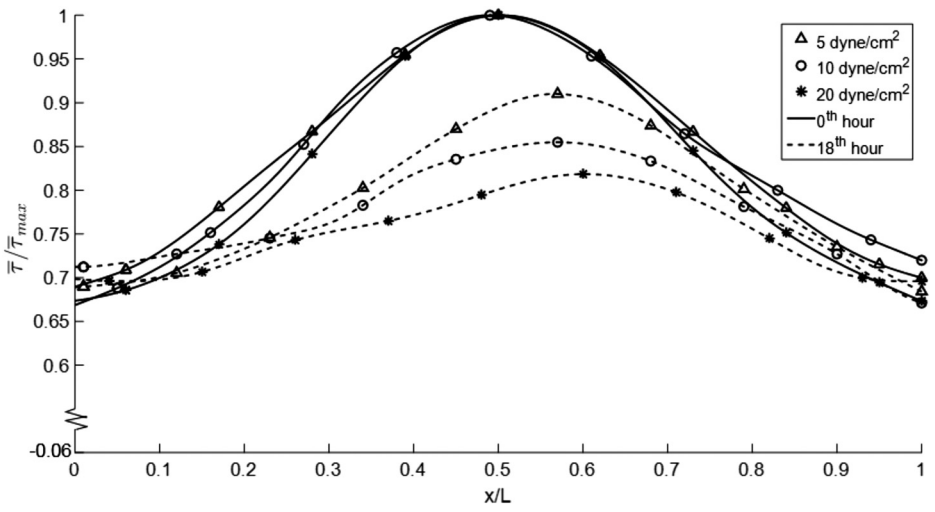


FIG. 12. Normalized average shear stress variations along the normalized streamwise cell length at the 0th and 18th hour time steps for a confluent layer of endothelial cells cultured on glass at applied shear stresses of 5, 10 and 20 dyn/cm$^2$. Flow is from left to right.

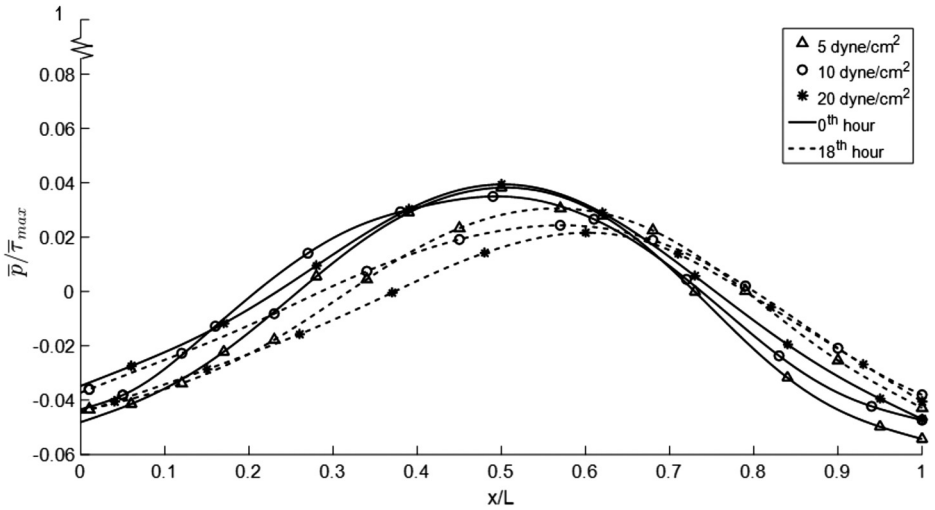


FIG. 13. Plots of averaged pressure non-dimensionalized by maximum initial shear stress as a function of position along the cells at the 0th and 18th hour.

The distribution of surface pressure along the ensemble average of cells was also computed. Results from these calculations are shown in Fig. 13. Again, profiles for the three different flows at the 0th and 18th hours are shown. For the complete pressure data set, the reader is referred to Lambert.[41]

As with the averaged shear stress distribution along the cells, pressure decreases with increasing applied shear and the location of the pressure maxima moves with the location of maximum thickness. What is of greatest interest, however, is the magnitude of the pressure *differentials* between the highest and lowest points of the cells in comparison to the shear stress differentials between the same locations. Before going into this, a quick aside is necessary to clarify the different contributions to "pressure" acting on individual endothelial cells, and why the pressure data in Fig. 13 are relevant.

It is important to recall that for this study, a gage pressure calculation was used; integration of the pressure gradient field used a zero-pressure boundary condition. In other words, the pressure calculation here does not include the blood pressure acting on the entire artery. In a physiological environment, the pressure variations presented in Fig. 13 would be superimposed on the arterial blood pressure where the cells are located. The systolic pressure will be orders of magnitude larger than the pressure levels measured in this study. The critical differentiator to be recognized at this juncture is that while the vascular pressure varies over distances that are many vessel diameters long, the viscous flow induced pressure shown here varies over individual cells. It is the coupled interaction of this viscous induced pressure field with the shear stress variations caused by the cell topography that is of particular interest here. A critically important topic for future study is the effect of hypertension on this pressure-shear coupling at the cellular level.

Returning, now, to the main thread of the discussion, a comparison of the shear stress differentials in Fig. 12 and pressure differentials in Fig. 13 shows that they are of the same magnitude. In general, the differential in pressure from the front (or back) of a cell to the point of maximum height is approximately 30% of the shear stress differential between the same locations. The primary takeaway at this point is that mechanotransduction is affected by pressure *as well as* shear stress and not shear alone. This validates the earlier finding[28] with the very important difference that this study has demonstrated mechanical response to applied fluid loading on live endothelial cells where the previous work drew a conclusion based on measurements over fixed cells. Furthermore, in this study, it was possible to quantify the response as a function of different shear stress environments.

### C. Notes on varying substrates and environmental conditions

As noted in the opening of this section, there were a number of different experiments that were conducted during this investigation. The primary data set reported here was obtained using

endothelial cells cultured directly on the glass micro-channel floor. A somewhat reduced set of experiments was done for cells cultured on the floor treated with fibronectin. Finally, additional earlier experiments were conducted using different lighting conditions and a different working fluid which, it turned out, caused cells to form vacuoles as a result of phototoxicity. Those cells would often undergo necrosis and frequently would not remain attached to the micro-channel for the full 18 h. While these experiments with phototoxic effects were physiologically meaningless, they did shed light on the similarity between the experiments conducted with and without a fibronectin substrate. This is highlighted in the following paragraphs.

One of the "universally accepted" responses of endothelial cells subjected to flow is that they will elongate and reorient themselves to align with the flow. The full mechanical response, then, would include (i) alignment of the cells to the flow direction, (ii) reduction in maximum height, and (iii) redistribution of cell topography such that the maximum height is located over the back half of the cell. To use a simplistic automotive metaphor, the transformation would be from the shape of a VW Beetle to a Formula I racecar. This concept of drag minimization has been discussed previously.[28,45]

As reported,[41] endothelial cell shape in the *x-y* plane, i.e., in the microscope viewing plane, was examined for all of the different experiments. The starting point for this analysis was the same edge detection algorithm used to ensemble average topography and stress distributions over the cells. This was described in Sec. II I. The output of this algorithm was a black and white image of the cells where the cells were white and regions between cells were black. Centroids and major and minor axes could be computed for each cell.

In looking at the cells cultured directly on glass, it was immediately obvious that the cells did not reorient even when subjected to the highest applied mean shear stress of 20 dyn/cm$^2$. The microscope images of the cells at the 0th hour and the 18th hour were identical irrespective of the applied shear stress level. The interpretation was that the cell adhesion to the glass was too strong to allow the cells to reorient in response to the applied flow. So, while the cells did reduce in height and "lean away" from the flow direction, the shape of the cells in contact with the wall did not change.

It was hypothesized that this might have been due to the fact that the cells were cultured directly on glass, a decidedly non-physiologic condition. For this reason, the glass micro-channel floor was coated with fibronectin before culturing cells. The rationale was that providing a more physiologic interface for the cells would allow the cells to exhibit the alignment and reorientation phenomenon observed in other studies.

To test this hypothesis, two different applied shear stresses, 5 dyn/cm$^2$ and 20 dyn/cm$^2$, were tested with the fibronectin substrate. The results, shown in Table I, were the same as those with the cases of culturing directly onto the glass floor. That is, within the uncertainties of the measurements,

TABLE I. Comparison of key topography and stress changes between endothelial cells cultured directly on the glass micro-channel floor and cells cultured with a fibronectin substrate. The center set of three columns shows the decrease in the three parameters, $h_{max}$, $\tau/\tau_{max\text{-}0hr}$, and $p/\tau_{max\text{-}0hr}$, between the maximum value in the 0th hour and the maxima at the 18th hour. The right hand set of three columns shows how far the maximum values shifted downstream (normalized with respect to the cell length) after being subjected to flow for 18 h.

| Applied shear (dyn/cm$^2$) | Substrate | Change in the maximum value from 0th to 18th hour | | | Downstream displacement of the maximum value from 0th to 18th hour; $\Delta(x/L)$ | | |
|---|---|---|---|---|---|---|---|
| | | $h_{max}$ ($\mu$m) | $\tau/\tau_{max\text{-}0hr}$ | $p/\tau_{max\text{-}0hr}$ | $h_{max}$ | $\tau/\tau_{max\text{-}0hr}$ | $p/\tau_{max\text{-}0hr}$ |
| 5 | Glass | −0.23 | −0.30 | −0.02 | +0.07 | +0.07 | +0.07 |
| | Fibronectin | −0.26 | −0.24 | −0.02 | +0.06 | +0.07 | +0.06 |
| 10 | Glass | −0.36 | −0.48 | −0.03 | +0.08 | +0.08 | +0.08 |
| | Fibronectin | … | … | … | … | … | … |
| 20 | Glass | −0.45 | −0.61 | −0.06 | +0.10 | +0.10 | +0.10 |
| | Fibronectin | −0.44 | … | … | +0.09 | … | … |

the data and trends in Figs. 7–13 were the same for the fibronectin cases. Furthermore, the cells cultured with a fibronectin substrate also did not elongate or align with the flow.

Table I highlights the comparison of key parameters in the cases with and without the fibronectin substrate. The change in maximum values of $h_{max}$, $\tau/\tau_{max\text{-}0hr}$, and $p/\tau_{max\text{-}0hr}$ between the 0th and 18th hours is shown along with the downstream shift in streamwise locations of the maximum values, $\Delta(x/L/$ over the same time interval for un-treated glass and fibronectin-coated experiments. Here, $\tau_{max\text{-}0hr}$ denotes the maximum local shear stress value over the ensemble average of cells at the 0th hour; this was located at the highest point on the cell initially at the cell mid-length, $x/L = 0.5$. Note that after it was determined that cells were also not aligning with the flow even with the fibronectin substrate, there was no attempt made to complete that data set.

This absence of reorientation and elongation was unexpected, though not completely unique. It was shown[22] that elongation and reorientation of bovine aortic endothelial cells subjected to shear flow could be inhibited by treating them with the permeable calcium ion chelator quin2-AM and the tyrosine kinase inhibitor herbimycin A. It is also possible[21–23] that the duration of the measurements may not have been sufficiently long to observe elongation and realignment. The reason why cells did not align with the flow in this study, however, is a topic of further study.

In the early stages of this investigation, the cells were illuminated throughout the experimental runs; there was not an understanding at that point of the phototoxic effects that could be induced by doing this. In addition, a series of experiments was conducted in which the pH of the working fluid was 6.7 as opposed to an optimal pH of 7.4 for endothelial cells. The same three applied shear stresses were studied, and outside of pH, all other experimental parameters were the same.[41]

The key feature of these experiments was that the cells underwent necrosis. As a consequence, a major topographical difference between these cells and the previously described healthy cell experiments is that the necrotic cells became *thicker* when subjected to flow. This is consistent with a study[29] including the evolution of endothelial cells undergoing apoptosis in response to contamination.

Of greater significance, however, is that the cells in this experimental set were observed to also migrate downstream and align with the flow with time. These phenomena were observed for all three applied shear flows. This is important because it is an indicator that there was not something about the micro-channel geometry or the culturing methodology that somehow forced the cells to unnaturally adhere to the microchannel floor irrespective of the substrate. Future work will then need to focus on this issue of cell adhesion to the substrate.

## IV. CONCLUSIONS

Spatially resolved $\mu$PTV measurements were made of flow over confluent layers of live, healthy bovine aortic endothelial cells subject to three steady laminar shear flows: 5, 10, and 20 dyn/cm$^2$. From these measurements, cell topography, shear stress, and pressure variations were computed over the cells at 3-h intervals over an 18 h period. Distributions of geometry and cell loading were ensemble averaged over multiple cells in each field of view to enable statistically significant statements about the response of cells to applied shear. The key findings from these experiments are

- cell height reduces with increasing levels of applied shear,
- the streamwise location of the highest point on the cells moves downstream with increasing shear,
- there is a lateral spreading of the cells as cell height decreases to maintain constant cell volume, and
- there is a concomitant decrease in maximum shear stress and pressure over the cells as their topography changes in response to the applied fluid loading.

This study demonstrates the ability to spatially and temporally quantify fluid forces and endothelial mechanics using $\mu$PTV techniques and fluid dynamics principles. This methodology creates the opportunity for broader investigations of the mechanotransduction related to vascular disease such as atherogenesis.

## ACKNOWLEDGMENTS

The authors would like to express their appreciation to Dr. Kenneth Bayles from UNMC for the use of the Bioflux system and to Ms. Jennifer Endres for her help with support and training for the Bioflux.

[1]D. Ku, D. Giddens, C. Zarins, and S. Glagov, "Pulsatile flow and atherosclerosis in the human carotid bifurcation: Positive correlation between plaque location and low and oscillating shear stress," Arteriosclerosis **5**, 293–302 (1985).
[2]J. Tarbell, "Mass transport in arteries and the localization of atherosclerosis," Annu. Rev. Biomed. Eng. **5**, 79–118 (2003).
[3]C. G. Caro, "Discovery of the role of wall shear in atherosclerosis," Arterioscler. Thromb. Vasc. Biol. **29**, 158–161 (2009).
[4]L. Cancel, A. Fitting, and J. Tarbell, "*In vitro* study of LDL transport under pressurized (convective) conditions," Am. J. Physiol. Heart Circ. Physiol. **293**, H126–H132 (2007).
[5]U. Olgac, V. Kurtcuoglu, and D. Poulikakos, "Computational modeling of coupled blood-wall mass transport of LDL: Effects of local shear stress," Am. J. Physiol. Heart Circ. Physiol. **294**, H909–H919 (2007).
[6]N. Sun, N. B. Wood, A. D. Hughes, S. Thom, and X. Xu, "Effects of transmural pressure and wall shear stress on LDL accumulation in the arterial wall: A numerical study using a multilayered model," Am. J. Physiol. Heart Circ. Physiol. **292**, H3148–H3157 (2007).
[7]J. M. Tarbell, "Shear stress and the endothelial transport barrier," Cardiovasc. Res. **87**, 320–330 (2010).
[8]N. Yang and K. Vafai, "Modeling of low-density lipoprotein (LDL) transport in the artery—effects of hypertension," Int. J. Heat Mass Transfer **49**, 850–867 (2006).
[9]L. Nielson, "Transfer of low-density lipoproteins (LDL) transport in the artery—effects of hypertension," Atherosclerosis **123**, 1–15 (1996).
[10]R. Ross, "Atherosclerosis—An inflammatory disease," N. Engl. J. Med. **340**, 115–126 (1999).
[11]J. C. Wang and M. Bennett, "Aging and atherosclerosis," Circ. Res. **111**, 245–259 (2012).
[12]L. S. Shankman, D. Gomez, O. A. Cherepanova, M. Salmon, G. F. Alencar, R. M. Haskins, P. Swiatlowska, A. A. C. Newman, E. S. Greene, A. C. Straub, B. Isakson, G. J. Randolph, and G. K. Owens, "KLF4-dependent phenotypic modulation of smooth muscle cells has a key role in atherosclerotic plaque pathogenesis," Nat. Med. **21**, 628–637 (2015).
[13]S. Skeoch and I. N. Bruce, "Atherosclerosis in rheumatoid arthritis: Is it all about inflammation?," Nat. Rev. Rheumatol. **11**, 390–400 (2015).
[14]D. R. Potter, J. Jiang, and E. R. Damiano, "The recovery time course of the endothelial cell glycocalyx *in vivo* and its implications *in vitro*," Circ. Res. **104**, 1318–1325 (2009).
[15]P. J. Butler, G. Norwich, S. Weinbaum, and S. Chien, "Shear stress induces a time- and position-dependent increase in endothelial cell membrane fluidity," Am. J. Physiol.: Cell Physiol. **280**, C962–C969 (2001).
[16]M. E. Rosenfeld, "Converting smooth muscle cells to macrophage-like cells with KLF4 in atherosclerotic plaques," Nat. Med. **21**, 549–551 (2015).
[17]M. DeBakey, G. Lawrie, and D. Glaeser, "Patterns of atherosclerosis and their surgical significance," Ann. Surg. **201**, 115–131 (1985).
[18]J. Flaherty, J. Pierce, V. Ferrans, D. Patel, W. Tucker, and D. Fry, "Endothelial nuclear patterns in the canine arterial tree with particular reference to hemodynamic events," Circ. Res. **30**, 23–33 (1972).
[19]R. Nerem, M. Levesque, and J. Cornhill, "Vascular endothelial morphology as an indicator of the pattern of blood flow," J. Biomech. Eng. **103**, 172–176 (1981).
[20]C. F. Dewey, Jr., S. Bussolari, M. Gimbrone, Jr., and P. Davies, "The dynamic response of vascular endothelial cells to fluid shear stress," J. Biomech. Eng. **103**, 177–185 (1981).
[21]M. Sato, M. Levesque, and R. Nerem, "Micropipette aspiration of cultured bovine aortic endothelial cells exposed to shear stress," Arteriosclerosis **3**, 276–286 (1987).
[22]A. Malek and S. Izumo, "Mechanism of endothelial cell shape change and cytoskeletal remodeling in response to fluid shear stress," J. Cell Sci. **109**, 713–726 (1996).
[23]C. Galbraith, R. Skalak, and S. Chien, "Shear stress induces spatial reorganization of the endothelial cell cytoskeleton," Cytoskeleton **40**, 317–330 (1998).
[24]P. Davies, A. Remuzzi, E. Gordon, C. F. Dewey, Jr., and M. Gimbrone, Jr., "Turbulent fluid shear stress induces vascular endothelial cell turnover *in vitro*," Proc. Natl. Acad. Sci. **7**, 2114–2117 (1986).
[25]G. Helmlinger, R. Geiger, S. Schreck, and R. Nerem, "Effects of pulsatile flow on cultured vascular endothelial cell morphology," J. Biomech. Eng. **113**, 123–131 (1991).
[26]S. Liu, M. Yen, and Y. C. Fung, "On measuring the third dimension of cultured endothelial cells in shear flow," Proc. Natl. Acad. Sci. **19**, 8782–8786 (1994).
[27]S. Q. Liu and Y. C. Fung, "Dependence of arterial remodeling on locally altered blood pressure," ASME Bioeng. Div. **29**, 59–60 (1995).
[28]A. V. Voorhees, G. B. Nackman, and T. Wei, "Experiments show importance of flow-induced pressure on endothelial cell shape and alignment," Proc. R. Soc. Lond. A **463**, 1409–1419 (2007).
[29]C. Leong, A. Voorhees, G. B. Nackman, and T. Wei, "Flow bioreactor design for quantitative measurements over endothelial cells using micro-particle image velocimetry," Rev. Sci. Instrum. **84**, 045109 (2013).
[30]Y. Sugii, "Simultaneous measurement of wall shear stress distribution and three-dimensional shape of living endothelial cells cultured in microchannel," J. Biomech. Sci. Eng. **5**, 625–634 (2010).
[31]S. S. Dol, M. M. Salek, K. D. Viegas, K. D. Rinker, and R. J. Martinuzzi, "Micro-PIV and CFD studies show non-uniform wall shear stress distributions over endothelial cells," in *Proceedings of the 8th International Conference on Nanochannels, Microchannels, and Minichannels* (ASME, 2010), pp. 31–39.
[32]P. Davies, "Flow-mediated endothelial mechanotransduction," Physiol. Rev. **75**, 519–560 (1995).
[33]P. Davies, K. Barbee, M. Volin, A. Robotewskyj, J. Chen, L. Joseph, M. Griem, M. Wernick, E. Jacobs, C. Polacek, N. DePaola, and A. Barakat, "Spatial relationships in early signaling events of flow-mediated endothelial mechanotransduction," Annu. Rev. Physiol. **59**, 527–549 (1997).

[34]R. Satcher, S. Bussolari, M. Gimbrone, Jr., and C. F. Dewey, Jr., "The distribution of fluid forces on model arterial endothelium using computational fluid dynamics," J. Biomech. Eng. **114**, 309–316 (1992).
[35]K. Barbee, T. Mundel, R. Lal, and P. Davies, "Subcellular distribution of shear stress at the surface of flow-aligned and nonaligned endothelial monolayers," Am. J. Physiol. **268**, H1765–H1772 (1995).
[36]P. Wache, X. Wang, G. Maurice, M. Lucius, and J. Stoltz, "Numerical computation of mechanical deformation of a modeled endothelial cell," C. R. Acad. Sci. IIb Mec. **328**, 633–638 (2000).
[37]C. Baquey, in *Biomechanical Transport Processes*, edited by F. Mosora, C. G. Caro, and H. Schmid-Schönbein (Springer, 1990).
[38]J. H. Dangaria and P. J. Butler, "Microrheology and adaptive microrheology of endothelial cells subjected to fluid shear stress," Am. J. Physiol. Physiol. **293**, C1568–C1575 (2007).
[39]B. P. Helmke, R. D. Goldman, and P. F. Davies, "Rapid displacement of vimentin intermediate filaments in living endothelial cells exposed to flow," Cell. Biol. **86**, 745–752 (2000).
[40]J. A. Frangos, T. Y. Huang, and C. B. Clark, "Steady shear and step changes in shear stimulate endothelium via independent mechanisms—superposition of transient and sustained nitric oxide production," Biochem. Biophys. Res. Commun. **224**, 660–665 (1996).
[41]L. M. Lambert, "Temporally and spatially resolved quantification of hemodynamic forces and endothelial mechanics," Ph.D. dissertation (Department of Mechanical and Materials Engineering, University of Nebraska–Lincoln, 2016).
[42]A. V. Voorhees, "Measurement of total mechanical loading on endothelial cells *in vitro* using micron-resolution particle image velocimetry," Ph.D. dissertation (Department of Mechanical and Aerospace Engineering, Rutgers University, 2004).
[43]J. Westerweel, "Efficient detection of spurious vectors in particle image velocimetry data," Exp. Fluids **16**, 236–247 (1994).
[44]J. Dabiri, S. Bose, B. Gemmel, S. Colin, and J. Costello, "An algorithm to estimate unsteady and quasi-steady pressure fields from velocity field measurements," J. Exp. Biol. **217**, 331–336 (2014).
[45]A. Hazel and T. Pedley, "Vascular endothelial cells minimize the total force on their nuclei," Biophys. J. **78**, 47–54 (2000).
[46]T. Ohashi, H. Sugawara, T. Matsumoto, and M. Sato, "Surface topography measurement and intracellular stress analysis of cultured endothelial cells exposed to fluid shear stress," Microbes Environ. **43**, 780–786 (2000).
[47]K. Barbee, P. Davies, and D. Lal, "Shear stress-induced reorganization of the surface topography of living endothelial cells imaged by atomic force microscopy," Circ. Res. **1**, 163–71 (1994).
[48]C. Chung and B. Min, "Fluid dynamic effects on endothelial cell morphology," in *Abstracts of the 3rd World Congress on Biomechanics* (Hokkaido University, Sapporo, 1998), p. 170.
[49]T. Pham, S. Maenz, C. Ludecke, C. Schmerbauch, U. Settmacher, K. Jandt, J. Bossert, and J. Zanow, "Quantitative characterization of endothelial cell morphologies depending on shear stress in different blood vessels of domestic pigs using a focused ion beam and high resolution scanning electron microscopy (FIB-SEM)," Tissue Cell **47**(**2**), 205–212 (2015).
[50]M. Levesque and R. Nerem, "The elongation and orientation of cultured endothelial cells in response to shear stress," J. Biomech. Eng. **107**, 341–347 (1985).
[51]C. Leong, "*In vitro* measurements of flow over endothelial cells," Ph.D. dissertation (Department of Mechanical, Aerospace, and Nuclear Engineering, Rensselaer Polytechnic Institute, 2008).
[52]M. C. Ferko, A. Bhatnagar, M. B. Garcia, and P. J. Butler, "Finite-element stress analysis of a multicomponent model of sheared and focally-adhered endothelial cells," Annu. Biomed. Eng. **35**, 208–223 (2007).